CrossMark

RESEARCH ARTICLE

Enhancement of synthetic schlieren image resolution using total variation optical flow: application to thermal experiments in a Hele-Shaw cell

Juvenal A. Letelier[1,2] · Paulo Herrera[1,2] · Nicolás Mujica[3] · Jaime H. Ortega[4,5]

Abstract We present an improvement to the standard synthetic schlieren technique to obtain the temperature distribution of a fluid inside of a Hele-Shaw cell. We aim to use the total variation L^1-norm optical flow method to treat experimental images and to obtain quantitative results of the development of thermal convection inside a cell, by detecting the gradients of the optical refractive index. We present a simple algorithm to set the optical flow parameters, which is based on the comparison between the optical flow output and the result obtained by digital PIV using the structural index metric. As an example of the application of the proposed method, we analyze laboratory experiments of thermal convection in porous media using a Hele-Shaw cell. We demonstrate that the application of the proposed method produces important improvements versus digital PIV, for the quantification of the gradients of the refractive index including the detection of small-scale convective structures. In comparison with correlation-based digital methods, we demonstrate the advantages of the proposed method, such as denoising and edge capture. These features allow us to obtain the temperature, for this experimental setting, with better image resolution than other techniques reported in the literature.

1 Introduction

Over the last few decades, many visualization and image processing techniques in experimental fluid dynamics have been proposed to describe qualitatively and quantitatively the behavior of certain flow regimes. The synthetic schlieren technique (SS) (Dalziel et al. 1998; Sutherland et al. 1999; Dalziel et al. 2000) has been used to study interesting fluid dynamics problems such as internal waves and stratification because of its simple implementation and the quality of the results that can be obtained. This technique is based on the detection of the apparent displacements of a synthetic background due to changes in the optical refractive index of the test fluid. Commonly, the computational method used to detect the apparent displacements is digital PIV (Raffel et al. 1998), a correlation-based image method which has subpixel accuracy but an image resolution of the order of the overlap times the interrogation window size. Moreover, some interesting mathematical techniques in image processing such as Lucas–Kanade, Horn–Schunck, and Brox optical flow methods (Horn and Schunck 1981; Lucas and Kanade 1981; Brox et al. 2004) have been applied in images obtained with the background-oriented schlieren technique (BOS) (Richard and Raffel 2001; Gojani and Obayashi 2012; Gojani et al. 2013; Raffel 2015), an optical visualization method similar to SS. The application of the mentioned optical flow methods

✉ Juvenal A. Letelier
juve.letelier.cl@gmail.com

1 Departamento de Ingeniería Civil, Facultad de Ciencias Físicas y Matemáticas, Universidad de Chile, Avenida Blanco Encalada 2002, Santiago de Chile, Chile

2 Centro de Excelencia en Geotermia de los Andes (CEGA), Facultad de Ciencias Físicas y Matemáticas, Universidad de Chile, Santiago de Chile, Chile

3 Departamento de Física, Facultad de Ciencias Físicas y Matemáticas, Universidad de Chile, Avenida Blanco Encalada 2008, Santiago de Chile, Chile

4 Departamento de Ingeniería Matemática, Facultad de Ciencias Físicas y Matemáticas, Universidad de Chile, Avenida Beauchef 851, Santiago de Chile, Chile

5 Centro de Modelamiento Matemático UMI 2807 CNRS, Facultad de Ciencias Físicas y Matemáticas, Universidad de Chile, Avenida Beauchef 851, Santiago de Chile, Chile

improves the image resolution in comparison with digital PIV (Atchenson et al. 2009). The same conclusion has been reported when another versions of optical flow method have been applied in particle tracking and velocimetry experiments (Ruhnau et al. 2005a, b; Ruhnau and Schnorr 2007).

All optical flow methods have an issue known as the aperture problem, which arises when a moving object is viewed through an aperture without the information of some structural properties such as edges, corners, and texture data (Wedel and Cremers 2011). Therefore, to avoid this problem, all optical flow methods require a regularization. Depending on the regularization used, optical flow can be formulated using a featured-based approach or a variational approach. In general, variational formulations have the best performance in statistical evaluations. One of these formulations, based on the introduction of a L^1-regularity term $\varepsilon_{reg} = |\nabla \mathbf{u}|$ (Rudin et al. 1992; Zach et al. 2007) and known as the total variation optical flow estimation (abbreviated as OpFlow), has shown to have interesting properties such as noise removal and the preservation of edges and contrast (Chan et al. 2001; Strong and Chan 2003). Therefore, OpFlow (Zach et al. 2007; Sanchez et al. 2013) is promising for analyzing results of physical experiments.

The Rayleigh–Benard convection (RBC) in porous media is a benchmark problem where many visualization techniques have been applied. RBC is of particular interest in research because it appears in a wide range of geophysical problems, including earth's mantle convection, geothermal energy extraction, and underground energy storage systems. In the laboratory scale, some experiments about RBC in porous media using analogue working fluids in Hele-Shaw cells have been widely reported in the literature (Elder 1967a, b; Hartline and Lister 1977; Koster and Muller 1982; Nield and Bejan 2006; Cooper et al. 2014). In this context, the use of passive dyes for the observation of streaklines (Horne and O'Sullivan 1974), the pH color indicator method (Hartline and Lister 1977), the holographic interferometry technique (Koster 1983; Lee and Kim 2004), thermal point measurements (Nagamo et al. 2002), and thermo-sensitive liquid crystals (Ozawa et al. 1992; Cooper et al. 2014) have been used to show the onset and the development of vertical thermal plumes that enhance heat transport inside the cell. However, the resolution of the images obtained with existing techniques is limited, and thermal details are commonly missing. Then, RBC in porous media using a Hele-Shaw cell is a good candidate to apply SS and to visualize thermal plumes.

In this work, we propose the use of OpFlow as an image analysis method for the SS technique, which gives better image resolution. To illustrate the applicability of OpFlow in optical density visualization, we implement the SS technique to quantify the temperature field inside a Hele-Shaw cell, where the working fluid has a temperature-dependent viscosity, and the cell is heated from below and cooled from above. The choice of studying heat transport in such type of fluids is motivated by the growing interest in understanding the physics of the geothermal energy extraction through carbon dioxide injection (Randolph and Saar 2011) and supercritical CO_2 storage in geological formations (Benson et al. 2005; Emami-Meybodi et al. 2015), where the viscosity is variable with the concentration of dissolved supercritical CO_2 into brine and only slightly variable with temperature.

The mathematical theory of OpFlow is discussed in Sect. 2. OpFlow depends on some non-physical free parameters which, in general, are chosen through visual inspection of the results. We determine these parameters by using a statistical methodology in which digital PIV plays a central role. The main goals and contributions of the article are (a) to use a statistical tool to define adequately the OpFlow parameters to analyze experimental images, using digital PIV as a preprocessing step, and (b) to quantify the refractive index gradients in the flow, in a wide range of spatial scales, using the discontinuity detection capabilities of OpFlow. The final contribution of this article is (c) to use OpFlow results to reconstruct the temperature map in stratified fluids in an out-of-equilibrium regime. Using these results, we demonstrate that the horizontal average temperature as a function of the vertical coordinate gives important information about the heat flux at the boundaries and the behavior of the convection inside the cell. In the following, we describe the mathematical theory of OpFlow.

2 Mathematical theory

2.1 Total variation optical flow

Optical flow is a mathematical method that quantifies the apparent motion of objects in space caused by the relative motion between a physical observer and the scene or by physical phenomena, such as particle motion or thermal convection (Baker et al. 2011). This idea was introduced by J. J. Gibson during the Second World War and played a key role in the development of the ecological approach to visual perception, an approach that emphasizes studying human perception in the natural environment. He defined optical flow as information carried by light resulting from environmental structure and the animal's path through the environment (Gibson 1950, 1966).

Let $I(\mathbf{x}, t_0)$ be the intensity of a fluid parcel in the location $\mathbf{x}$ at time t_0, and $I(\mathbf{x} + \mathbf{u}(\mathbf{x}), t_1)$ be the intensity of the same parcel at time t_1, which will have displaced in space. The quantity $\mathbf{u}(\mathbf{x}) = (u, w)$ is the two-dimensional displacement field (or optical flow field) that has to be determined.

The most important assumption of optical flow is that the intensity value of the parcel $I(\mathbf{x}, t_0)$ does not change while it moves to $I(\mathbf{x} + \mathbf{u}, t_1)$, which is known as the brightness constancy assumption (BCA), and it is represented by the equation

$$-\frac{\partial I}{\partial t} = \nabla I \cdot \mathbf{u} \tag{1}$$

which contains two unknowns, u and w, that cannot be solved; thus, it is necessary to introduce an additional regularity constrain. To regularize the problem, Horn and Schunck (1981) introduced a smoothness term by penalizing the derivative of the optical flow field, yielding a functional which must be minimized using a variational approach

$$F[\mathbf{u}] = \int_\Omega \left(|\nabla \mathbf{u}|^2 + \lambda |\vartheta(\mathbf{u})|^2 \right) d\Omega \,,$$
$$\vartheta(\mathbf{u}) = \frac{\partial I}{\partial t} + \nabla I \cdot \mathbf{u} \tag{2}$$

where $\vartheta(\mathbf{u})$ imposes the BCA constrain to Eq. (2). The introduction of the quadratic L^2-regularizer $\varepsilon_{\text{reg}} = |\nabla \mathbf{u}|^2$, called spatial coherence, favoring flow fields which are spatially smooth, penalizing the high variations. Therefore, this quadratic regularizer does not allow the detection of discontinuities in the optical flow field (Wedel and Cremers 2011). The quadratic L^2-regularity present in the Horn–Schunck functional might not be a regularizer based on physical approaches. A first-order div-curl L^2-regularizer of the type $\varepsilon_{\text{reg}} = \alpha |\nabla \cdot \mathbf{u}|^2 + \beta |\nabla \times \mathbf{u}|^2$ was introduced by Suter (1994), and a second-order div-curl L^2-regularizer $\varepsilon_{\text{reg}} = \alpha |\nabla(\nabla \cdot \mathbf{u})|^2 + \beta |\nabla(\nabla \times \mathbf{u})|^2$ has been proposed by Gupta and Prince (1996), where both have a much more physical meaning, penalizing high divergence-rotational components. However, the first- and second-order div-curl methods are more difficult to implement computationally (Corpetti et al. 2005; Stark 2013). A well-known limitation of the Horn–Schunck method is that it can only estimate small motions. In spite of the problem mentioned above, the method has been well evaluated (Meinhardt-Llopis et al. 2013) and the variational formulation (2) allows us to compute the optical flow field for all pixels within the image, resulting in a dense flow field (one vector per pixel). This feature is attractive since it does not require subpixel algorithms to estimate the apparent displacement through the position of the maximum in the correlation plane, such as for digital PIV. Despite the fact that the accuracy of the subpixel level in PIV is 0.1 to 0.05 pixels, the image resolution obtained in SS by using cross-correlation methods is of the order of the size of the interrogation window scaled with the overlap used (one vector per window), which is 8×8 pixels in the most general case. Moreover, the computational costs of using OpFlow are more expensive than digital PIV.

In general, in real-world scenes and laboratory-scale experiments, there may be many objects with defined edges moving. Because of that, some authors change the quadratic L^2-regularity to a L^1-regularity which better preserves discontinuities (Wedel and Cremers 2011). In this context, the total variation optical flow method (OpFlow) is a variational method whose formulation is based on the minimization of the functional given by Zach et al. (2007)

$$J[\mathbf{u}] = \int_\Omega \left(|\nabla \mathbf{u}| + \lambda |\psi(\mathbf{u})| \right) d\Omega \,,$$
$$\psi(\mathbf{u}) = I(\mathbf{x} + \mathbf{u}_0, t_1) + \nabla I(\mathbf{x} + \mathbf{u}, t_1) \cdot (\mathbf{u} - \mathbf{u}_0) - I(\mathbf{x}, t_0) \,, \tag{3}$$

which is the L^1 version of Horn–Schunck functional (2), where $\psi(\mathbf{u})$ is called the residual (BCA data term), $\mathbf{u}_0$ is an approximation of $\mathbf{u}$ and λ is a parameter known as the attachment parameter (Sanchez et al. 2013). Despite the fact that there are many versions of L^1-regularity terms proposed in the literature, we have chosen the OpFlow formulation given by Zach et al. (2007) because they have proposed an exact numerical scheme to solve (3) by using the well-known Rudin–Osher–Fatemi (ROF) model, which has denoising capabilities without blurring edges (Rudin et al. 1992) . This point is important, because we want to detect not only discontinuities on the flow, but also get a smooth flow where noise is controlled. The TV-L^1 method, which means total variation with the L^1-norm, is used to compute the integral over the domain of the absolute values of mathematical quantities of interest. In Eq. (3), the objective quantity to minimize is the L^1-norm of the gradient of the flow subject to the L^1-norm of the BCA data term, which is controlled by the parameter λ. An efficient method given by Zach et al. (2007), which uses the duality-based method proposed by Chambolle (2004), solves Eq. (3). The method enables one to find the minimum of the strictly convex functional with a quadratic relaxation

$$J_\theta[\mathbf{u}] = \int_\Omega \left(|\nabla \mathbf{u}| + \frac{1}{2\theta} (\mathbf{u} - \mathbf{v})^2 + \lambda |\psi(\mathbf{v})| \right) d\Omega \,, \tag{4}$$

where $\mathbf{v}$ is an auxiliary vector (known as the dual variable), and the parameter θ is known as the tightness parameter (Sanchez et al. 2013). Setting the parameter θ to a small value, it forces J_θ to reach its minimum value when $\mathbf{u} \sim \mathbf{v}$, obtaining the TV-$L^1$ functional (3). Although the optical flow is rigorous and accessible to further developments, there is a certain ambiguity in the correct choice of parameters λ and θ that represent the apparent motion of an experimental image pair and the computation of dense motion fields. The choice of both parameters is often a practical problem in the application of OpFlow to analyze physical experiments.

If an exact representation of the flow is known (the ground truth image), some popular performance

estimators such as the angular error, the average end-point error, the interpolation error, and the normalized interpolation error (Barron et al. 1994; Baker et al. 2011) help to set λ and θ. However, in experimental images, this information is not known a priori, and the choice by inspection of the parameters is a common practice. To solve this problem, we propose to use digital PIV as a preprocessing step. The idea is to compare the results of both techniques, digital PIV and Opflow, by using the structural similarity index metric (Wang et al. 2004; Wang and Bovik 2009). We associate the highest value of this metric with the optimal values for λ and θ for the image in study, so that the initial image resolution obtained with digital PIV can be improved by the dense flow field given by OpFlow. As well as the Horn–Schunck optical flow, the resolution of OpFlow is equal to one pixel. As a consequence, OpFlow can detect small structures of few pixels of length with a better definition, while globally structural properties are similar to those obtained by digital PIV (see Fig. 9 for more details).

The OpFlow method has been extensively evaluated against other optical flow methods (Barron et al. 1994; Baker et al. 2011) using the average end-point error over some images of the Middlebury database, obtaining better results in comparison with Lucas–Kanade, Horn–Schunck, and Brox algorithms which have been used in the BOS literature (Atchenson et al. 2009). In particular, an interesting extension given by Wedel et al. (2008) which uses a cartoon-texture image decomposition by the $TV\text{-}L^1$ model improves the BCA constrain and therefore the optical flow estimation. In our experimental applications, it is not necessary to use this decomposition because the conditions of illumination of the cell are homogeneous along experimental runs.

2.2 Statistical metrics

In order to compare the similitude between two images, the mean square error (MSE) has been used in signal processing applications. If f and g are two images represented as a two-dimensional array of size $N_x \times N_y$, the MSE metric between them is defined as

$$\text{MSE} = \frac{1}{N_x N_y} \sum_{i=1}^{N_x} \sum_{j=1}^{N_y} \left[f_{j,i} - g_{j,i} \right]^2 . \tag{5}$$

Therefore, a minimum value of MSE means a good similarity between images. In addition, the structural similarity index metric (SSIM) is defined as

$$\text{SSIM} = \frac{(2\mu_f \mu_g + C_1)(2\sigma_{fg} + C_2)}{(\mu_f^2 + \mu_g^2 + C_1)(\sigma_f^2 + \sigma_g^2 + C_2)} , \tag{6}$$

where, if the image is stored as a one-dimensional array of size $N = N_x N_y$, the mean intensity and the standard deviation of the image f are defined as

$$\mu_f = \frac{1}{N} \sum_{s=1}^{N} f_s \; ; \; \sigma_f = \sqrt{\frac{1}{N-1} \sum_{s=1}^{N} \left[f_s - \mu_f \right]^2} .$$

In equation (6), C_1 and C_2 are constants. The SSIM metric satisfies the conditions of symmetry, boundedness (SSIM ≤ 1) and unique maximum (SSIM $= 1$ if and only if $f = g$). Wang and Bovik (2009) compare both metrics with a series of images distorted from an original image, concluding that the MSE values are nearly identical, even though the same images present important visual differences that are detected using SSIM. This conclusion is important in the comparison of our experimental images, so we analyze the data with the SSIM method instead of MSE.

2.3 Synthetic schlieren equations

The synthetic schlieren (SS) method is a non-intrusive, optical density visualization technique in fluid mechanics that measures the optical refractive index gradients of a test fluid by means of the quantification of the deflections of the light rays that come from a background image (Dalziel et al. 2000).

The SS equation, in the simplified one-dimensional problem, can be obtained minimizing the optical length functional (Kumar and Muralidhar 2012)

$$F[y] = \int_0^L n(y) \sqrt{1 + \left(\frac{\mathrm{d}y}{\mathrm{d}z} \right)^2} \, dz, \tag{7}$$

where $y = y(z)$ is the vertical deflection of the light ray in function of the horizontal variable z, as shown in Fig. 1, and $n = n[y(z)]$ is the optical refractive index of the fluid, which depends on space. The Euler–Lagrange equation associated with (7) is

$$n(y) \frac{\mathrm{d}^2 y}{\mathrm{d}z^2} = \left[1 + \left(\frac{\mathrm{d}y}{\mathrm{d}z} \right)^2 \right] \frac{\mathrm{d}n}{\mathrm{d}y}, \tag{8}$$

in which boundary conditions are associated with the physical problem to be solved. We assume that the optical system satisfies the paraxial approximation $dy/dz \ll 1$. If n is constant, the solution of Eq. (8) is a straight line $y(z) = y_i - z \tan \phi_i$, where $\tan \phi_i$ is the angle of the incident light ray. In a more general case, assuming that $n[y(z)] = n_f - n'[y(z)]$, where n_f is the reference refractive index of the fluid at temperature T_0, $n' \ll n_f$ and dn'/dy varies slowly with coordinate y, the solution of Eq. (8) is

$$y(z) = y_i - z \tan \phi_i - \frac{1}{2n_f} \frac{\mathrm{d}n'}{\mathrm{d}y} z^2 . \tag{9}$$

The paraxial approximation is satisfied when $\phi_i \leq 10°$. In such case, $\tan \phi_i \sim \phi_i$ is valid within an accuracy of 1 %. From Fig. 1, reconstructing the light ray trajectory from A' to a', we have

Fig. 1 Light ray deflection due to a variable optical refractive index $n(y)$. The optical system is a Hele-Shaw cell made of acrylic. There are three physical media where light rays can travel, which are air, acrylic and the test fluid. The corresponding optical refractive indexes are n_a, n_p and $n(y)$, respectively. The points F and T are the focal length of the lens and the intersection of the apparent (incident, *dashed blue line*) and refracted (*dashed red line*) light rays

$$y_{a'} = y_{A'} - L_s \alpha - 2 L_p \frac{n_a}{n_p} \alpha - b \frac{n_a}{n_f} \alpha - L_c \alpha , \tag{10}$$

where n_a, n_p and n_f are the optical refractive index for air, acrylic, and the test fluid reference, respectively, and α is the incident paraxial angle in the position A'. This result is satisfied by a light ray that comes from the background image, when the system is unperturbed. Finally, reconstructing the light ray trajectory from A' to b' and defining the apparent displacement on the lens position $\Delta y_{a'b'} = y_{a'} - y_{b'}$, we obtain the well-known SS formula (Dalziel et al. 2000)

$$\Delta y_{a'b'} = \frac{b}{n_f} \frac{dn'}{dy} \left[\frac{1}{2} b + \frac{n_f}{n_p} L_p + \frac{n_f}{n_a} L_c \right] , \tag{11}$$

where the angle of deflection ε, formed by the incident and the refracted light rays (see Fig. 2), is defined as

$$\varepsilon = \frac{b}{n_a} \frac{dn'}{dy} . \tag{12}$$

Finally, using geometric operations, we obtain the apparent displacement on the background image $\Delta y_{AB} = y_B - y_A = s_t \varepsilon$, where s_t is the parallel distance to the optical axis between the background image and the intersection point of the light rays perturbed and unperturbed, as shown in Fig. 2, which is defined as

$$s_t = \frac{n_a}{n_f} \left[\frac{1}{2} \left(\frac{2n_f}{n_a} - 1 \right) b + \frac{n_f}{n_p} \left(\frac{2n_p}{n_a} - 1 \right) L_p + \frac{n_f}{n_a} L_s \right] .$$

This distance defines an effective refractive plane where light rays are deflected by local changes in the optical refractive index.
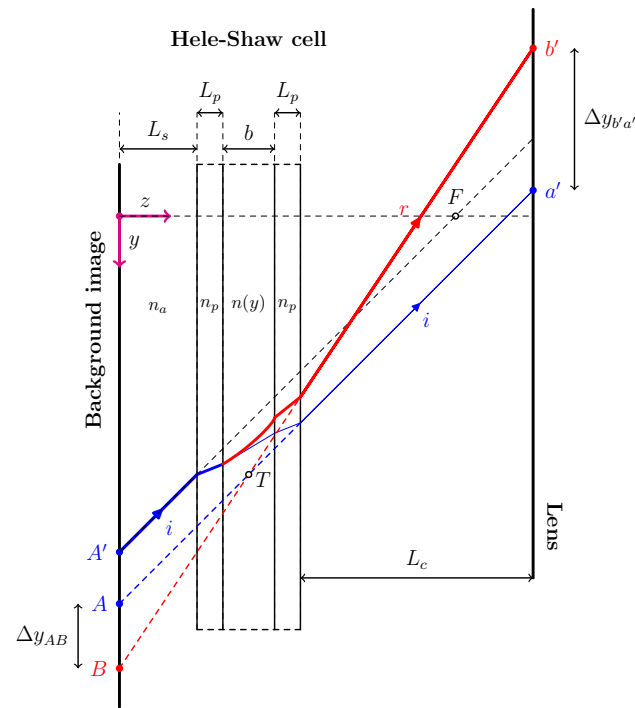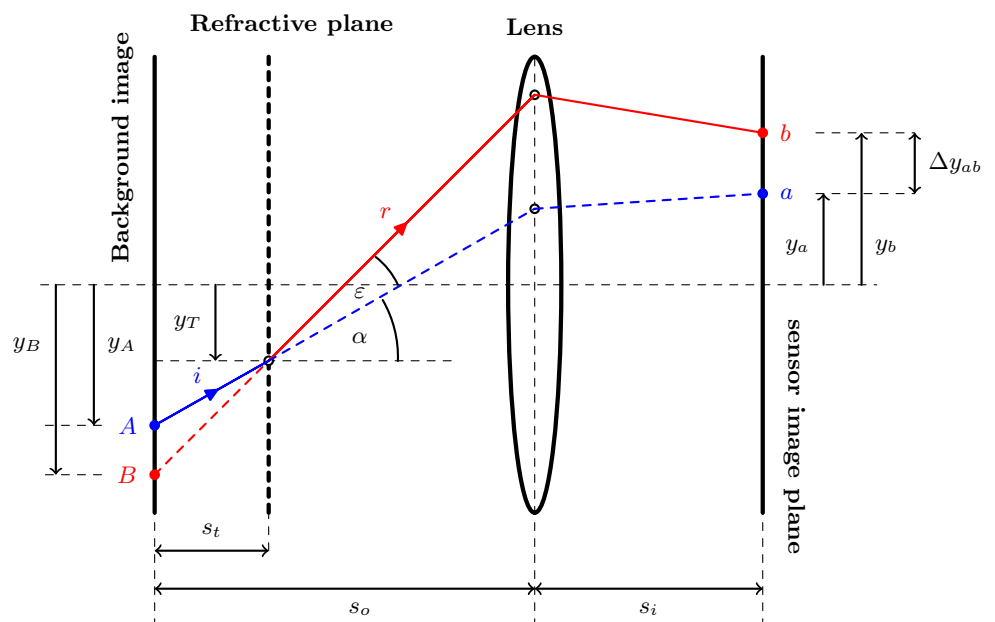

Fig. 2 Synthetic schlieren experiment setup. The image is a one-dimensional representation, where $\Delta y_{ba} = (\Delta x, \Delta y)$. The deflection angle ε is the angle between the refracted and the incident light rays (Gojani et al. 2013)

Let $M = s_i/s_o$ be the lens magnification. Using the thin lenses law, we have $M = f/(s_o - f)$, where f is the focal length, and s_o is the distance between the background image and camera, so the apparent displacement measured in the plane of the image sensor is $\Delta y_{ab} = M \Delta y_{AB}$. Replacing these relations in the definition of Δy_{AB}, we obtain

$$\varepsilon = \frac{\Delta y_{ab}}{M s_t}, \tag{13}$$

recovering the definition of the angle of deflection ε proposed by Gojani et al. (2013), in the context of image recording using the background-oriented schlieren (BOS) technique. In general, the SS and BOS techniques quantify a scalar property of the fluid, such as the density ρ, which depends on the thermodynamic variables through a constitutive equation. For example, if the fluid is air, then the Gladstone–Dale model and the ideal gas equation are applied successfully when BOS is used (Richard and Raffel 2001). In our experiments, a Hele-Shaw cell filled with pure PPG is heated from below and cooled from above with constant temperature difference $\Delta T = T_{bot} - T_{top}$. Then, a constitutive equation $n = n(T)$ is necessary to reconstruct the thermal dynamics, so the equation to solve is

$$\frac{dn'}{dy} = \frac{n_a}{b} \varepsilon(y), \tag{14}$$

which constitutes the mathematical formulation for the simplified one-dimensional model. If the deflection of the light ray has two-dimensional components, given by $\varepsilon = \varepsilon_x \hat{x} + \varepsilon_y \hat{y}$, the equations for the angles of deflection are

$$\varepsilon_x = \frac{\Delta x (s_0 - f)}{f s_t}, \quad \varepsilon_y = \frac{\Delta y (s_0 - f)}{f s_t}, \tag{15}$$

where Δx and Δy are the spatial deflections in the plane of the image sensor. Traditionally, these deflections are estimated from classical PIV algorithms (Tokgoz et al. 2012) or optical flow estimation, where the Lucas and Kanade (1981), Horn and Schunck (1981), and Brox et al. (2004) algorithms have been applied to experimental images giving satisfactory results (Atchenson et al. 2009). Here, we show that it is possible to enhance the detection of deflections by using OpFlow. Finally, Eq. (14) is extended to the vector model $\nabla n' = n_a \varepsilon(\mathbf{x})/b$, where taking the divergence on both sides of equation, we obtain the Poisson equation for SS–BOS techniques

$$\nabla^2 n' = \frac{n_a}{b} \nabla \cdot \varepsilon(\mathbf{x}), \tag{16}$$

with Neumann boundary conditions $\hat{x} \cdot \nabla n' = 0$ in $x = 0$ and $x = L$, in addition to the Dirichlet boundary conditions which are $n'(y = 0) = n'_{bot}$ and $n'(y = H) = n'_{top}$. Equation (16) will be used to reconstruct the temperature map for a

$Ra = 680$, which is presented in Sect. 5. To solve (16), we implement the Red-Black SOR-Chebyshev method (Press et al. 2007) using OpenMP libraries. In the following, we discuss the experimental setup and the application of OpFlow to analyze experimental images.

3 Experimental setup

3.1 Working fluid properties

Analogue fluids that represent a physical phenomenon in underground systems have been used in the context of supercritical CO_2 dissolution in brine-saturated porous media (Neufeld et al. 2010). In this context, Backhaus et al. (2011) used aqueous solutions of propylene glycol (PPG) as working fluid. The PPG shows interesting thermodynamical properties with important changes in temperature (Sun and Teja 2004). For the SS technique, the important variable to consider is the change in the optical refractive index as function of temperature. For the working fluid in consideration, this dependency is modeled as $n(T) = n_0 - \beta T$, where $n_0 = 1.4391$ and $\beta = 0.0003 \, °C^{-1}$ (Turan et al. 2002).

The density and dynamic viscosity of PPG were obtained from Sun and Teja (2004). Figure 3 shows the dependence with temperature for both fluid properties. This information will be used later to explain the results from visualization of temperature maps. For the experimental results shown in Sect. 5, the Prandtl number $Pr = \nu/\kappa$, where $\nu = \mu/\rho$ is the kinematic viscosity, is $Pr = 275$. Furthermore, the working temperatures were $T_{min} = 30 \, °C$ and $T_{max} = 45 \, °C$, as shown in Fig. 13.

3.2 Experimental setup and procedures

The experimental setup and methodology used for the acquisition of images are similar to those described in Wildeman et al. (2012) and suggested by Gojani et al. (2013) (see Fig. 2). The homogeneous porous medium is represented by a Hele-Shaw cell, which is made with acrylic of height $H = 100$ mm, width $L = 150$ mm, and thickness $L_p = 8$ mm. To separate the plates, we use two aluminum shims of width $\tilde{L} = 150$ mm, height $\tilde{H} = 30$ mm, and thickness $b = 1$ mm, sealing the cell on the top and bottom by pressing the plates and shims with stainless steel bolts. On the sides, the cell is sealed using O-rings which are pressed by other acrylic plates using bolts of similar characteristics, creating an experimental device which is waterproof (see Fig. 4).

The design of the Hele-Shaw cell leaves a free flow channel of dimensions $L \times h \times b$, with $h = 50$ mm. The cell is filled with propylene glycol from an inflow point,
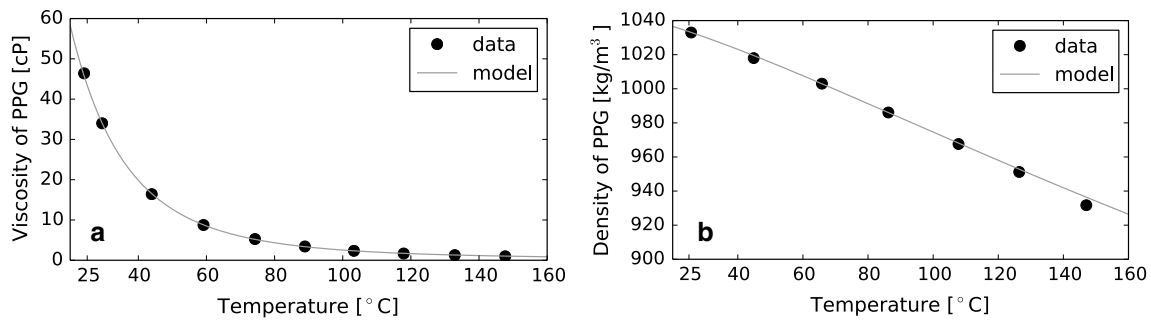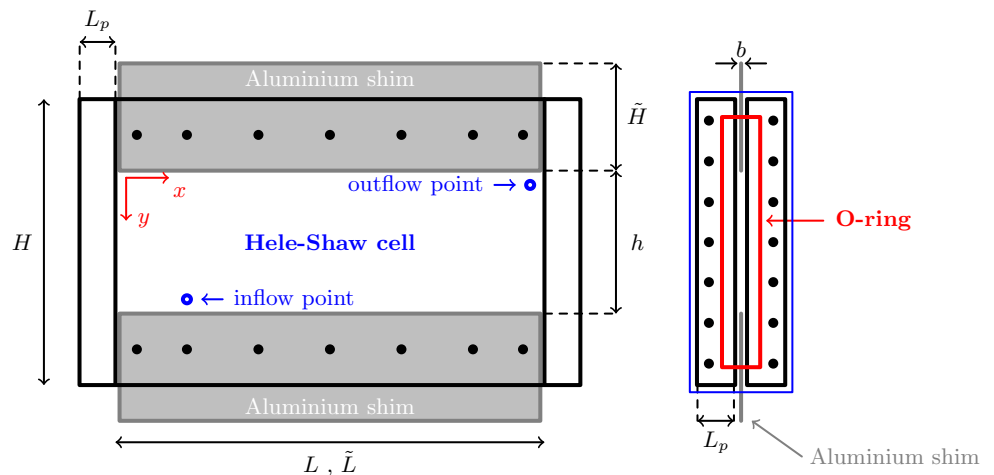
Fig. 3 **a** Dynamic viscosity of PPG as a function of temperature. **b** Density of PPG as a function of temperature. Experimental data were extracted from Sun and Teja (2004)

Fig. 4 Schematic view of the Hele-Shaw cell. The dimensions of variables presented in this figure are the following: $L = \tilde{L} = 150$ mm, $H = 100$ mm, $L_p = 8$ mm, $\tilde{H} = 30$ mm, $h = 50$ mm and $b = 1$ mm

saturating the flow channel, where excess fluid goes to a head tank through an outflow point. To generate the thermal convection, we add two nichrome wires on the free sides of aluminum shims, applying a constant current. The temperature on the shims is measured using both a RTD-PT100 sensor connected to a Keithley nano-voltmeter and a thermal camera ULIRvision, which confirms that the aluminum shims are heated uniformly, so we consider that the measured temperature on shims is the boundary conditions in which thermal convection can develop inside the cell. The convective behavior is controlled by the Rayleigh number $Ra = \Delta \rho g K H / \mu \kappa$ (Otero et al. 2004), where $\Delta \rho$ is the maximum density difference, g is the gravitational acceleration, $K = b^2/12$ is the permeability of the cell, b is the gap of the cell, H is the height, μ is the dynamic viscosity, and κ is the thermal diffusivity. With this information, for the experimental results shown in Sect. 5, we have $Ra = 680$.

3.3 Visualization and error analysis

To mount the experiment, we use an optical table and a metallic structure where the cell is inserted vertically. A white light LED panel is placed behind the cell, and a white acrylic light diffusor is placed between the cell and the LED panel. At the diffusor, we add a background pattern of dots printed on a transparent slide, creating the background image shown in Fig. 5.

Accordingly with Fig. 2, the SS configuration of the experiments is given by the parameters s_t, s_o and f. For the results presented in Sect. 4, we have $L_s = 5$ cm and $s_o = 100$ cm. A Canon Rebel T3 EOS camera was used to acquire photographs of size 5184×3456 pixels^2. The
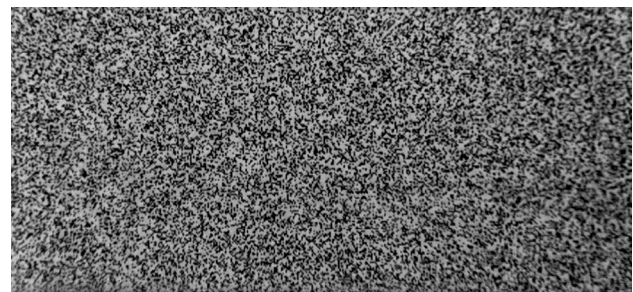

Fig. 5 Background dots pattern for BOS measures. The size of the image is 10×5 cm^2

images were saved using the 8-bit JPEG format since our main objective was to detect apparent displacements of synthetic dots of appreciable size. The 14-bit RAW format is very expensive in terms of data storage for our purposes. As we demonstrate in Sect. 4, the use of a lossy codec is adequate to accomplish our objectives.

The image focus was achieved by using a telephoto lens Canon EF 75–300 mm $f/4 - f/5.6$, and the focal length was set to $f = 135$ mm with a focal ratio $f_r = 5.6$. It is important to note that any issue from the CMOS sensor of the camera such as photon shot noise, pixel vignetting, and fill fraction of pixels can be avoided by the OpFlow denoising capabilities when images are analyzed. However, non-uniform response due to the photon shot noise can impact negatively in the CMOS sensor performance and therefore in the BCA constrain, limiting the applicability of OpFlow. In such cases, preprocessing the images using the cartoon-texture decomposition can be useful to fix this problem (Wedel et al. 2008). In this work, this preprocessing step was not used because the original images are adequate to be analyzed directly with OpFlow.

Following Gojani et al. (2013), an experiment is well suited for the application of SS when the fluid flow only deflects the light ray, but does not displace it. From Fig. 2, this condition is satisfied when $b/(s_o - s_t) = 1 \times 10^{-3} \ll 1$, which is fulfilled by our experimental setup. Moreover, the background image dimensions must satisfy the condition $\max\{L/2, H/2\} \leq s_o/4$ to ensure the paraxial limit assumed in Eq. (14). In our experiments, we have $L/2 = 10$ cm and $H/2 = 5$ cm.

The optical refractive index values considered in this work are $n_a = 1.00029$, $n_p = 1.49$ and $n_f = 1.4331$ at $T = 20\,°C$. Considering that the cell lengths were measured using a vernier of resolution 0.01 mm and the cell gap was measured using a micrometer of resolution 0.001 mm, we

have $s_t = 61.28 \pm 0.03$ mm. The error in the estimation of ε can be computed using the formula $\sigma_\varepsilon = \delta/[2(s_o - f)]$, where δ is the diameter of a single dot in the background image. By construction, $\delta = 100$ µm and $\sigma_\varepsilon = 6 \times 10^{-5}$ rad. A single pixel of the CMOS camera sensor is equivalent to 1 pixel $= 91.95 \pm 0.09$ µm of the background image, so by using the angular error σ_ε and the maximum displacement detected by OpFlow, which is $\Delta y_{ab}^{(max)} = 5.5$ pixels, we have $\Delta y_{AB}^{(max)} = 0.506 \pm 0.004$ mm. The error of this estimation is the spatial resolution of the optical system in our experiments. Obviously, the spatial resolution can be enhanced by two ways, reducing the dot diameter or increasing the distance s_o and magnification.

4 Optical flow results

4.1 Displacement sensibility analysis

The OpFlow algorithm and libraries given by Sanchez et al. (2013), modified for automation and data storage purposes using python libraries and HDF5, were applied to the acquire images. As an example of this application, for a fixed $\lambda = 0.1$ and variable θ, we obtain the image sequence presented in Fig. 6, where the displacement $D_{OF}(\theta, \lambda) = \sqrt{\mathbf{u} \cdot \mathbf{u}}$, detected by OpFlow formula (4), depends on θ. For very small θ, the method does not detect changes in the pair of images, but for very large θ values, the flow is over smoothed.

By visual inspection of the sequence presented above, we conclude that the best image resolution was achieved for $O(\theta) \sim 1$. Figure 7 shows $\max[D_{OF}]$ as function of θ, for several values of λ. It is interesting to note that $\max[D_{OF}]$ always has a local maximum for $10^{-4} < \theta < 10^2$ and
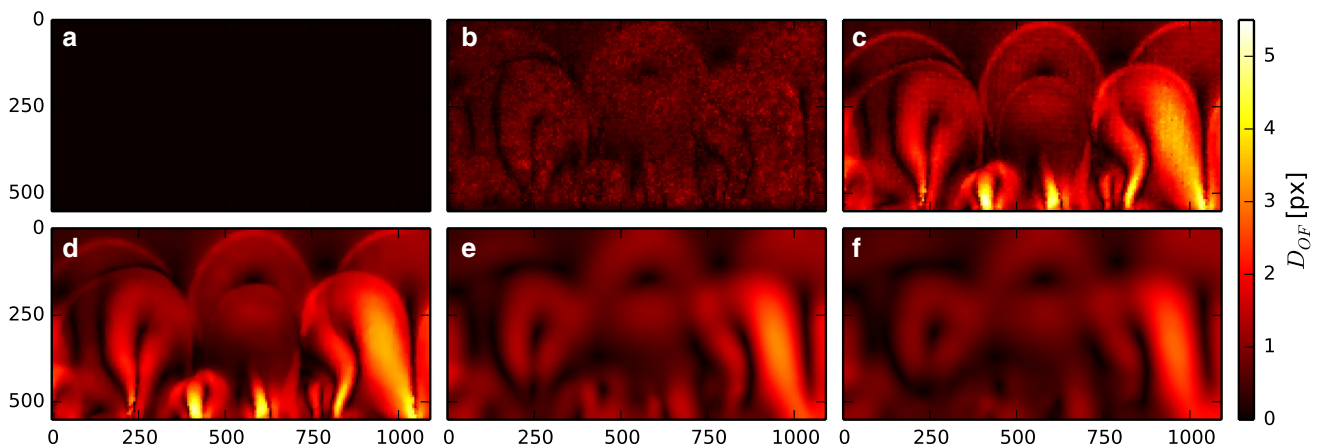

Fig. 6 OpFlow results for $\lambda = 0.1$ and different values of θ: $\theta = 1 \times 10^{-4}$ (**a**), $\theta = 1 \times 10^{-2}$ (**b**), $\theta = 1 \times 10^{-1}$ (**c**), $\theta = 1$ (**d**), $\theta = 1 \times 10^2$ (**e**) and $\theta = 1 \times 10^4$ (**f**). With the objective to compare the size of the image and the maximum displacement detected by OpFlow, the *vertical* and *horizontal* coordinate values in each image are given in pixels. The conversion is 550 pixels = 50 mm
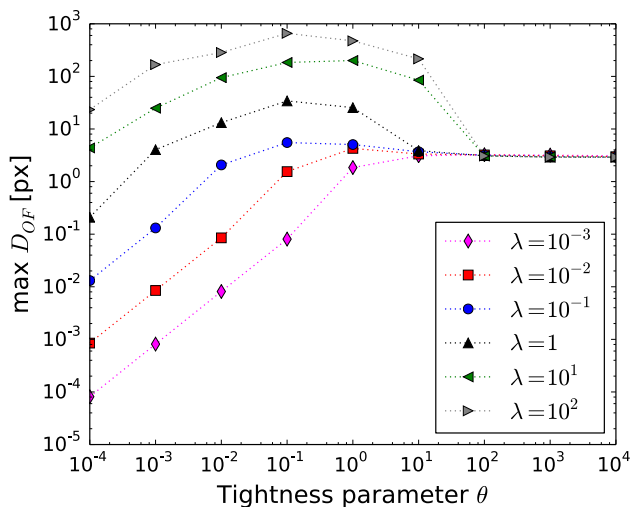
Fig. 7 Sensitivity analysis of OpFlow parameters, using the maximum displacement detected as the metric. It is interesting to note that this metric reaches a constant value for $\theta > 10^2$, which is independent of λ

$\lambda > 10^{-2}$. Moreover, $\max[D_{OF}]$ reaches a constant value for $\theta > 10^2$, which is clearly observed in Fig. 6e, f, where the images appear diffused in comparison with others.

Considering these results for $\max[D_{OF}]$, the principal problem that arises when OpFlow is applied is the correct choice of optimal parameters. When the exact flow is not known, there is no ground truth image to compare with, so that the choice of parameters must be done by visual inspection. Physically, the method loses strength when it is compared with other techniques such as digital PIV, which detects a correct maximum displacement. Moreover, digital PIV is not adequate when cross-correlation is poor. In this sense, it is reasonable to think that there is a compromise between a good correlation of a pair images (digital PIV) and the generation of dense fields (OpFlow), which can be used to analyze image motion with high accuracy. In the following, we will explain the application of the statistical metrics defined above, to obtain an approximation of the adequate values of OpFlow parameters using a digital PIV preprocessing, where we want to compute an initial result of the apparent displacement, which is later enhanced by means of the OpFlow estimation.

4.2 Comparison between digital PIV and OpFlow

OpenPIV (Liberzon et al. 2009) is an open-source software that implements the cross-correlation algorithm given in Raffel et al. (1998), using fast Fourier transform (FFT) and standard statistical tools for vector validation. Setting the interrogation window $w = 16$ pixels, the overlap as $50\,\%$ and the well-known peak to peak as a signal-to-noise method with thresholding of 1.8, the maximum displacement detected by the method is $\max[D_{PIV}] = 5.4$

pixels $= 0.497$ mm. To compare the OpFlow and digital PIV results using OpenPIV, the statistical metric defined in Eq. (6) gives the mathematical background to establish a methodology to fix the Opflow parameters. This methodology consists in finding the maximum value of the SSIM metric for several scales of λ and θ. As an example, we use the same data set used to generate the maps shown in Fig. 6, and we compute the SSIM for an array of 13×13 values of λ and θ. A quadratic bivariate spline is applied to the scatter data, generating the smoothed and continuous map shown in Fig. 8b. The maximum value SSIM $= 0.684$ is achieved for $\lambda_c = 0.029$ and $\theta_c = 1.072$, where the position of this point is shown in Fig. 8a.

Therefore, the λ and θ values found using SSIM are chosen as the OpFlow parameters, giving the results shown in Fig. 9, which is similar to the visual inspection parameter estimation and where a significant improvement with respect to the digital PIV result is observed. It is interesting to note that the OpFlow result is denoised, capturing the small-scale displacements that are hidden in the digital PIV result. Moreover, the result of the application of the SSIM metric to both image methods gives a small θ_c, so the proposed method effectively recover an important feature of Chambolle's method (Chambolle 2004) and λ is converted to the important parameter in OpFlow, because it controls the accuracy of the method. There is no theoretical method to determine the optimal values of both parameters from OpFlow equation. However, the empirical results from this kind of experiments suggest that the statistical methodology allows the definition of a good set of OpFlow parameters that ensures a good representation of the observed physical phenomena. For experimental image sequences, the methodology can be automated and the OpFlow parameters can be computed for each image. As example, we observe that OpenPIV took about 30 s to analyze an image of 622×1341 pixels in a MacBook Pro with an Intel Core i7 2.2 GHz processor, while the methodology using SSIM is a time-consuming process, taking about 15 min to analyze the same image. However, computing these parameters for a few images and calculating the mean values, we obtain a reasonable strategy to optimally set λ and θ. Once that has been done, the OpFlow parameters are set globally for each image. Using OpenMP libraries, the time execution of the OpFlow algorithm is approximately 30 s.

To evidencing the capabilities of OpFlow in the edge detection and image denoising, on the right image of Fig. 10, it is possible to appreciate an horizontal boundary structure on the bottom zone of the image, which corresponds to the aluminum shim. This boundary is not detected by OpenPIV, as shown on the left image of Fig. 10. Additionally, the noise result obtained with OpenPIV is typical of cross-correlation methods applied to SS experiments, and it is due to the image resolution of the
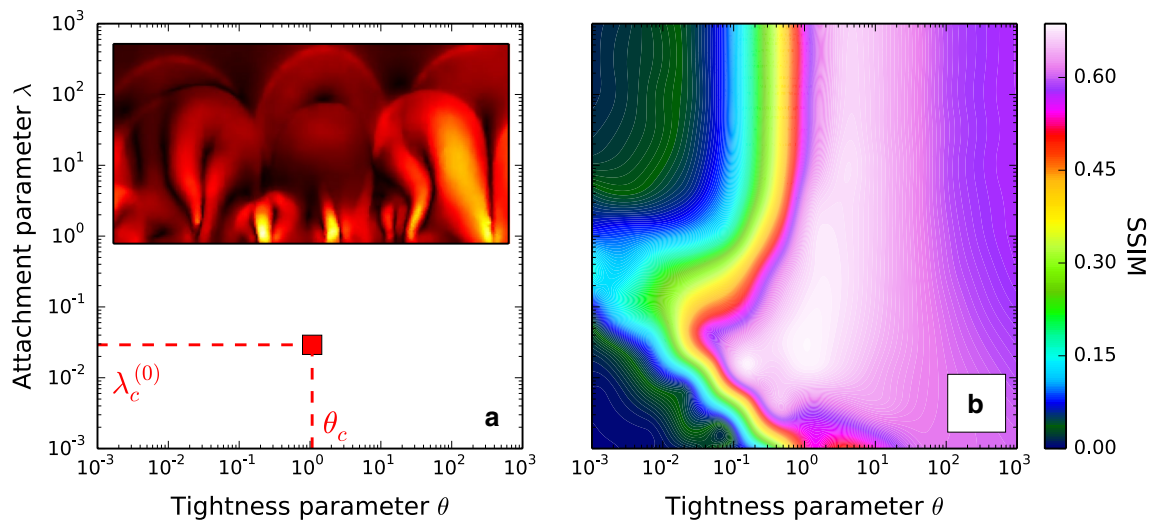
Fig. 8 SSIM parameter space. The statistical strategy enables to define adequately the OpFlow parameters. The maximum value of SSIM was achieved for $\lambda_c = 0.029$ and $\theta_c = 1.072$ which is indicated by the *square dot* in (**a**). As a result, the smooth OpFlow output using these parameter values is showed in the *inset* plot in (**a**). This plot is discussed in Fig. 9. **b** Shows the characteristic values of SSIM parameter space for the image pair analyzed. The structure of the SSIM parameter space is not universal and depends on the images
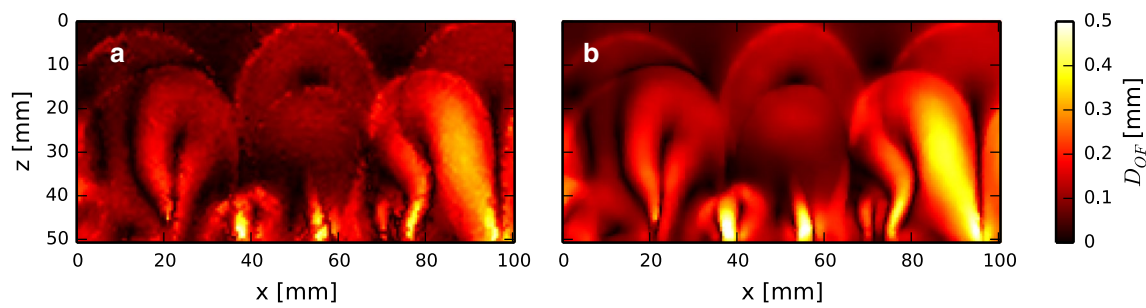
Fig. 9 OpenPIV **a** compared with OpFlow result **b** for the apparent displacement of background dots pattern. The OpFlow image was generated using the parameters $\lambda = 0.029$ and $\theta = 1.072$. A significant improvement of the resolution of the displacement was achieved using OpFlow, in comparison with OpenPIV
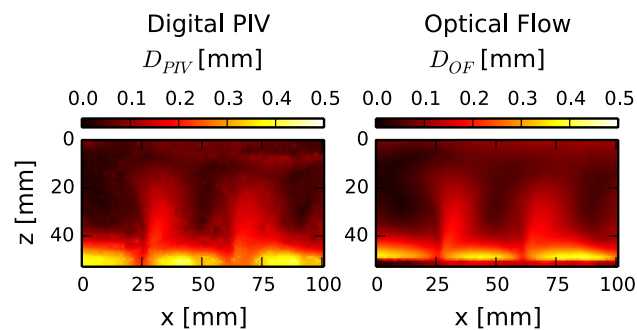
Fig. 10 OpenPIV compared with OpFlow for the apparent displacement of background dots pattern, for an experiment where $f = 55$ mm, $f_r = 7.1$, $b = 1$ mm, $L_p = 8$ mm, $L_s = 100$ mm and $s_o = 403$ mm. The OpFlow parameters are $\lambda = 0.02$ and $\theta = 2.48$

method, where we use an interrogation window of $w = 16$ pixels with an overlap of 50 %. On the other hand, OpFlow removes the noise, preserving the edges detected and improving the image resolution.

5 Thermal reconstruction

To reconstruct the thermal distribution, we use the mathematical theory presented in Sect. 2.3 and the numerical strategy to solve the differential equation of the SS theory, where the temperatures at bottom and top of the cell are constants. Figure 11 shows the result of the reconstruction of temperature from the apparent displacement on the background image shown on the right image of Fig. 10.

Fig. 11 Thermal reconstruction of the OpFlow result presented on the right image of Fig. 10. The *horizontal*-averaged temperature is shown with *error bars*, which is compared with the conductive regime. A deviation from the conductive regime is evidenced by means of the difference in the areas *below* the *curve*
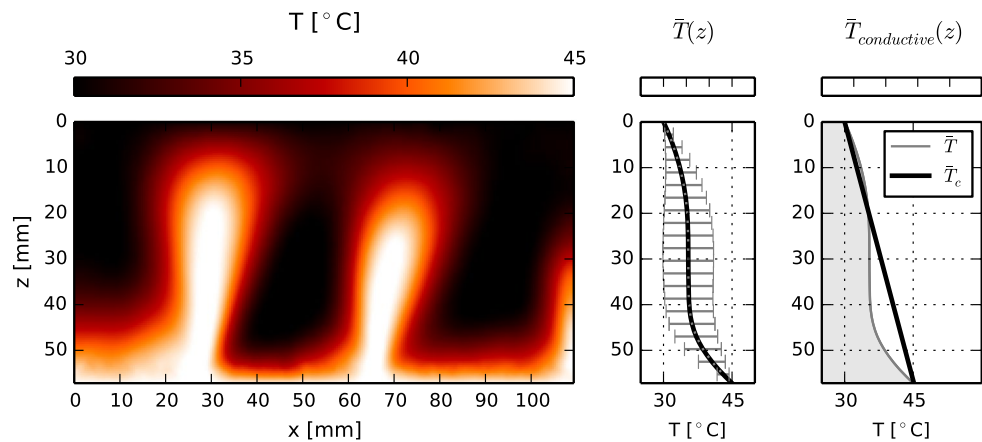
In this figure, we observe few convective isolated plumes. The conductive heat transfer is characterized by a stable temperature gradient in the whole domain, where the temperatures at $z = 0$ and $z = H$ are the temperatures measured at the aluminum shims. The same figure shows the horizontally averaged temperature versus depth, $\bar{T}(z,t) = (1/L) \int_0^L T(\mathbf{x},t)\,dx$. $\bar{T}(z)$ has a constant value in the middle of the cell with constant standard deviation, which is a behavior observed in developed thermal convection in porous media (Otero et al. 2004).

However, it is interesting to note that the values of $\partial \bar{T}/\partial z$ are different at the vertical boundaries, which can be explained considering the variability of the dynamic viscosity of the fluid with temperature and the heat lost due to thermal conduction through the solid walls. In fact, the viscosity of PPG at 30 °C is 32 cP, while this value at 45 °C is 15 cP, which is an important difference compared with the viscosity of water in the same range of temperatures. Defining the heat available per horizontal unit length as $Q_L^{(av)} = (1/L) \int_V \bar{\rho}\, c_p\, T\, dV = \bar{\rho}\, c_p\, b \int_0^H \bar{T}\, dz$, where $\bar{\rho}$ is the mean density between the range of temperatures considered, we see that the area below the curve of the observed $\bar{T}(z)$ is less than the theoretical curve for the purely conductive case. Considering $c_p = 2.51$ J/g K and $\bar{\rho} = 1.023 \pm 0.007$ g/cm^3, where the error is related with the deviation from the mean value for a range of temperatures between 30 and 45 °C, we obtain $\Delta Q_L = Q_L^{(conv)} - Q_L^{(cond)} = -(2.63 \pm 0.02)$ J/cm.

Thus, we have experimental evidence that some heat was conducted through the acrylic used to built the cell. This finding arises the question of how this heat transfer affects the convective behavior of the fluid. This question has also been studied by Koster (1983), concluding that the acrylic affects the thermal convection, so the new question is what is the amount of heat lost by conduction and how the heat lost scales with Ra, for this kind of experiments.

The thermal conductivity of acrylic is similar to that of PPG, which is $k_{ppg} = 0.195 \pm 0.001$ W/mK (Sun and Teja 2004). The error is related with the deviation from the mean value for a range of temperatures between 30 and 60 °C. To understand the energetic balance in thermal convection between the fluid and the acrylic, we analyze a transient convection regime for $Ra = 680$. The choice of this value is related with the observations of the geothermal convection in sedimentary basins (Clausnitzer et al. 2001).

Another example of thermal reconstruction is shown in Fig. 12. We can see many thermal plumes, where some nonlinear behaviors such as the coalescence and destabilization of protoplumes in the bottom boundary layer are evidenced. These processes are triggered by parcels of denser fluid that reach the lower regions of the cell and cause the convergence of parcels of less dense fluid. Due to viscosity effects, the dense fluid parcels move slowly in comparison with lighter fluid, so the observed nonlinear behavior is not only driven by density, but also by viscosity.

6 Transient dynamics

The transient regime is controlled by the temperature rise of the aluminum shims, which is slow. It takes about one hour to reach a constant temperature, as shown in Fig. 13. Because the top and bottom boundaries have temperatures that change with time, the lower zone of the cell shows the appearance of a boundary layer that destabilizes in a few thermal fingers, as we show in Fig. 12. This result is a good example that shows the transition to a fully developed convective dynamics, where the convection is driven by density and viscosity.

Figure 14 shows the conductive flux at vertical boundaries, where the conductive flux per unit length is computed as $\dot{Q}_L = k_{ppg}\, b\, \partial \bar{T}/\partial z$, being k_{ppg} the thermal conductivity of PPG. From this figure, we can observe that the heat flux at the bottom has a local minimum at $t = 50$ min, which coincides with the beginning of the destabilization of the thermal boundary layer. We define the mean value of a horizontal-averaged physical quantity $\bar{f}(z,t)$
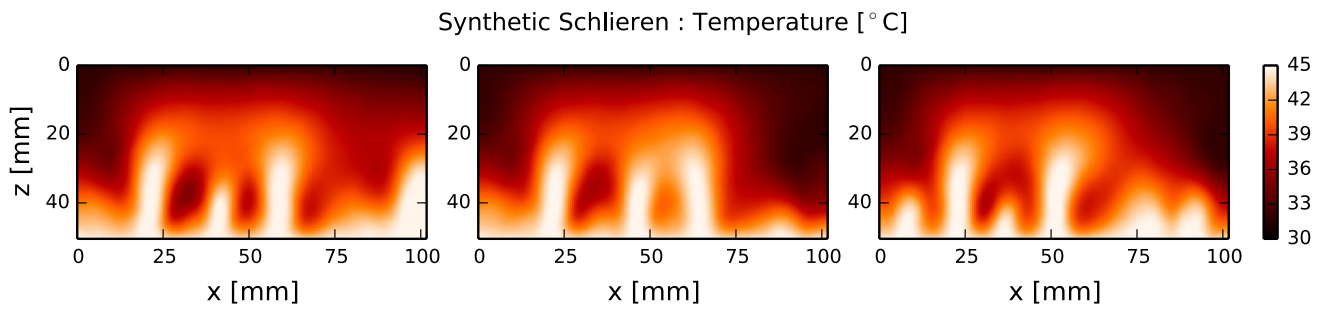
Synthetic Schlieren : Temperature [°C]

Fig. 12 Thermal reconstruction for an experimental image sequence for $Ra = 680$. The time difference between images is $\Delta t = 5$ min, from *left* to *right*. Some well-known nonlinear behaviors such as coalescence and destabilization of protoplumes can be observed
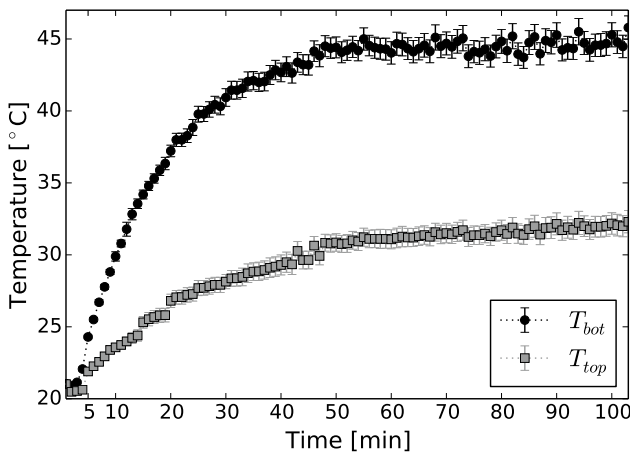

Fig. 13 Temperatures of the aluminum shims, on *bottom* T_{bot} and *top* T_{top}. These measurements were used as boundary conditions for thermal reconstruction in the transient regime
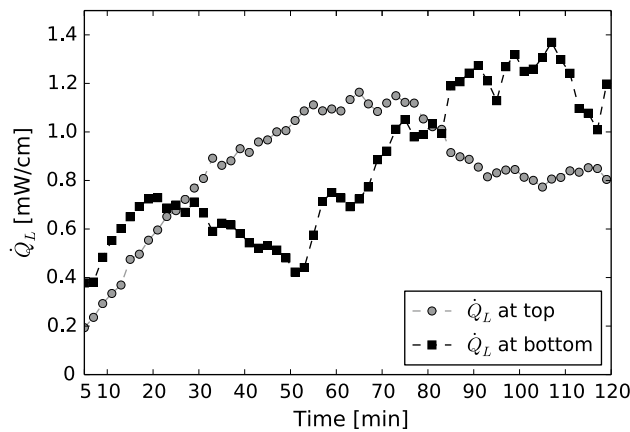
Fig. 14 Conductive heat flux per unit length, at *bottom* and *top* of the cell, during the transient regime

as $\langle f \rangle(t) = (1/H) \int_0^H \bar{f}(z,t)\, dz$. From Fig. 12, analyzing the mean temperature evolution presented in Fig. 15, we can observe that this quantity grows monotonically in
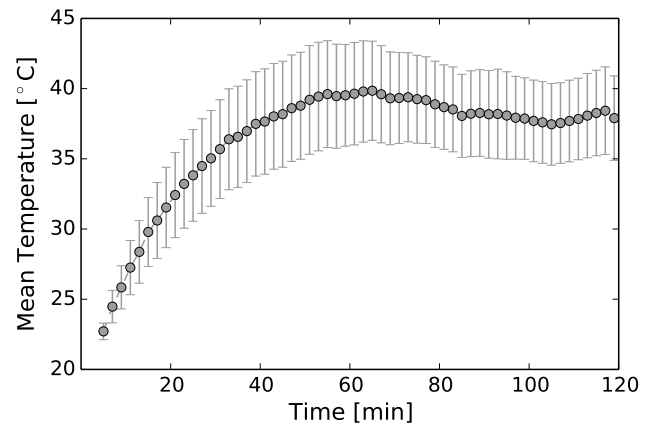

Fig. 15 Mean temperature $\langle T \rangle$ as function of time. We can see that the temporal evolution of this quantity seems to have a statistically constant value from the time $t = 80$ min

the transient regime, until it reaches an statistically constant value of $\langle T \rangle = 37.9 \pm 0.3\,°C$ from time $t = 80$ min. In other words, the system reaches a steady-state regime from this time, where the amplitude and shape of thermal plumes seem to be similar. Therefore, neglecting viscous dissipation and thermal dispersion, a first conclusion from the temperature reconstruction is that the difference between the conductive heat flux at top and bottom, from time $t = 80$ min (see Fig. 14), can be explained if we take into account the energy lost by wall conduction.

The total amount of energy injected to the fluid is used mainly in two processes, (a) to locally increase the temperature of the fluid, i.e., $\partial T/\partial t \neq 0$, and (b) to exchange energy with the solid walls by conduction. The estimation of the amount of mechanical energy converted into heat is important for the correct interpretation of the energy balance of the system. The results obtained from the temperature maps, for this regime, are not sufficient to conclude any effect from the dynamic viscosity in the development of thermal fingers, and more information is need to characterize the dynamics of the flow under these conditions.

7 Conclusions

We present a methodology based on the use of the $TV\text{-}L^1$ optical flow method (OpFlow) to analyze experimental images obtained by the SS technique. Comparing the images analyzed by digital PIV and OpFlow, we can estimate the optimal OpFlow parameters for a specific set of experimental images, improving the image resolution. As a benchmark case study where SS can be applied successfully in the measurement of a scalar quantity, in this case the temperature, we perform laboratory experiments of thermal convection in porous media, using a Hele-Shaw cell filled with propylene glycol as working fluid. The main advantages of the methodology to capture refractive index gradients using OpFlow are both image denoising and edge detection, which are crucial for further analysis of reconstructed temperature maps. We provide results that show these capabilities of OpFlow for the analysis of this type of experiments. These results are impossible to obtain using digital PIV, despite the fact that the correlation methods can be enhanced using a smoothing post-processing.

Using the dense flow field given by OpFlow, we reconstruct the temperature map for an experimental transient regime, and we study the conductive heat flux per unit length and the mean temperature as function of time, observing that the developed convection reaches a steady-state regime. Qualitatively, our thermal measurements show that the thermal boundary layer at the bottom destabilizes after a transient time. Above this boundary layer, heat transport is enhanced by a vertical advective flux that must be quantified. A work related with this problem is in progress. We will measure simultaneously both the temperature and velocity fields in order to better characterize the fluid dynamics of this type of systems.

References

Atchenson B, Heidrich W, Ihrke I (2009) An evaluation of optical flow algorithms for background oriented schlieren imaging. Exp Fluids 46:467–476. doi:10.1007/s00348-008-0572-7

Backhaus S, Turitsyn K, Ecke R (2011) Convective instability and mass transport of diffusion layers in a Hele-Shaw geometry. Phys Rev Lett 106(104):501. doi:10.1103/PhysRevLett.106.104501

Baker S, Scharstein D, Lewis JP, Roth S, Black MJ, Szeliski R (2011) A database and evaluation methodology for optical flow. Int J Comput Vis 92:1–31. doi:10.1007/s11263-010-0390-2

Barron J, Fleet D, Beauchemin S (1994) Performance of optical flow techniques. Int J Comput Vis 12:43–77

Benson S, Cook P et al (2005) Underground geological storage. In: Metz B, Davidson O, de Coninck H, Loss M, Meyer L (eds) Special report on carbon dioxide capture and storage, chap 5, Cambridge University Press, Cambridge, pp 195–276

Brox T, Bruhn A, Papenberg N, Weickert J (2004) High accuracy optical flow estimation based on a theory for warping. In: Pajdla T, Matas J (eds) Proceedings of 8th European conference on computer vision, 4, Springer, Berlin, pp 25–36

Chambolle A (2004) An algorithm for total variation minimization and applications. J Math Imaging Vis 20:89–97

Chan TF, Osher S, Shen J (2001) The digital TV filter and nonlinear denoising. IEEE Trans Image Process 10:231–241. doi:10.1109/83.902288

Clausnitzer V, Bayer U, Fuhrmann J (2001) Large-scale thermal convective instability in sedimentary basins. Eur Geophys Soc, Geophys Res Abstracts HS02-02

Cooper C, Crews J, Schumer R, Breitmeyer R, Voepel H, Decker D (2014) Experimental investigation of transient thermal convection in porous media. Transp Porous Media 104:335–347. doi:10.1007/s11242-014-0337-0

Corpetti T, Heitz D, Arroyo G, Memin E, Santa-Cruz A (2005) Fluid experimental flow estimation based on an optical flow scheme. Exp Fluids 40:80–97. doi:10.1007/s00348-005-0048-y

Dalziel SB, Hughes GO, Sutherland BR (1998) Synthetic schlieren. In: Proceedings of the 8th international symposium on flow visualization, Sorrento, pp 62.1–62.6

Dalziel SB, Hughes GO, Sutherland BR (2000) Whole field density measurements by synthetic schlieren. Exp Fluids 28:322–335. doi:10.1007/s003480050391

Elder J (1967a) Steady free convection in a porous medium heated from below. J Fluid Mech 27:29–48. doi:10.1017/S0022112067000023

Elder J (1967b) Transient convection in a porous medium. J Fluid Mech 27:609–623. doi:10.1017/S0022112067000576

Emami-Meybodi H, Hassanzadeh H, Green CP, Ennis-King J (2015) Convective dissolution of CO_2 in saline aquifers: progress in modeling and experiments. Int J Greenh Gas Control. doi:10.1016/j.ijggc.2015.04.003

Gibson J (1950) The perception of visual surfaces. Am J Psychol 63(3):367–384

Gibson J (1966) The problem of temporal order in stimulation and perception. J Psychol 62(2):141–149

Gojani AB, Obayashi S (2012) Assesment of some experimental and image analysis factors for background oriented schlieren measurements. Appl Opt 51:7554–7559. doi:10.1364/AO.51.007554

Gojani AB, Kamishi B, Obayashi S (2013) Measurement sensitivity and resolution for background oriented schlieren during image recording. J Vis 16:201–207. doi:10.1007/s12650-013-0170-5

Gupta SN, Prince JL (1996) Stochastic models for DIV-CURL optical flow methods. IEEE Signal Process Lett 3:32–34

Hartline BK, Lister RB (1977) Thermal convection in a Hele-Shaw cell. J Fluid Mech 79:379–389. doi:10.1017/S0022112077000202

Horn B, Schunck B (1981) Determining optical flow. Artif Intell 17:185–203. doi:10.1016/0004-3702(81)90024-2

Horne RN, O'Sullivan MJ (1974) Oscillatory convection in a porous medium heated from below. J Fluid Mech 66:339–352. doi:10.1017/S0022112074000231

Koster JN (1983) Interferometric investigation of convection in plexiglass boxes. Exp Fluids 1:121–128. doi:10.1007/BF00272010

Koster JN, Muller U (1982) Free convection in vertical gaps. J Fluid Mech 125:429–451. doi:10.1017/S0022112082003425

Kumar P, Muralidhar K (2012) Schlieren and shadowgraph methods in heat and mass transfer. Springer, New York. doi:10.1007/978-1-4614-4535-7

Lee S, Kim S (2004) Application of holographic interferometry and 2D PIV for HSC convective flow diagnostics. Meas Sci Technol 15:664. doi:10.1088/0957-0233/15/4/008

Liberzon A, Gurka R, Taylor Z (2009) Openpiv home page. [Online]. http://www.openpiv.net

Lucas B, Kanade T (1981) An iterative image registration technique with an application to stereo vision. In: Proceedings of seventh international joint conference on artificial intelligence, Vancouver, pp 674–679

Meinhardt-Llopis E, Sánchez J, Kondermann D (2013) Horn–Schunck optical flow with a multi-scale strategy. Image Process On Line 3:151–172. doi:10.5201/ipol.2013.20

Nagamo K, Mochida T, Ochifuji K (2002) Influence of natural convection on forced horizontal flow in saturated porous media for aquifer thermal energy storage. Appl Therm Eng 22:1299–1311. doi:10.1016/S1359-4311(02)00056-X

Neufeld J, Hesse M, Riaz A, Hallworth M, Tchelepi H, Huppert H (2010) Convective dissolution of carbon dioxide in saline aquifers. Geophys Res Lett 37(L22):404. doi:10.1029/2010GL044728

Nield D, Bejan A (2006) Convection in porous media, 3rd edn. Springer, New York. doi:10.1007/978-1-4614-5541-7

Otero J, Dontcheva L, Jonhston H, Worthing R, Kurganov A, Petrova G, Doering C (2004) High-Rayleigh-number convection in a fluid-saturated porous layer. J Fluid Mech 500:263–281. doi:10.1017/S0022112003007298

Ozawa M, Muller U, Kimura I (1992) Flow and temperature measurement of natural convection in a Hele-Shaw cell using a thermo-sensitive liquid-crystal tracer. Exp Fluids 12:213–222. doi:10.1007/BF00187298

Press WH, Teukolsky SA, Vetterling WT, Flannery BP (2007) Numerical recipes 3rd edition: the art of scientific computing, 3rd edn. Cambridge University Press, New York

Raffel M (2015) Background-oriented schlieren (BOS) techniques. Exp Fluids 56:1–17. doi:10.1007/s00348-015-1927-5

Raffel M, Willert C, Kompenhans J (1998) Particle image velocimetry. A practical guide, 2nd edn. Springer, Berlin. doi:10.1007/978-3-540-72308-0

Randolph JB, Saar MO (2011) Coupling carbon dioxide sequestration with geothermal energy capture in naturally permeable, porous geologic formations: Implications for CO_2 sequestration. Energy Procedia 4:2206–2213. doi:10.1016/j.egypro.2011.02.108

Richard H, Raffel M (2001) Principle and applications of the background oriented schlieren BOS method. Meas Sci Technol 12:1576. doi:10.1088/0957-0233/12/9/325

Rudin LI, Osher S, Fatemi E (1992) Nonlinear total variation based noise removal algorithms. Physica D 60:259–268. doi:10.1016/0167-2789(92)90242-F

Ruhnau P, Schnorr C (2007) Optical Stokes flow estimation: an imaging-based control approach. Exp Fluids 42:61–78. doi:10.1007/s00348-006-0220-z

Ruhnau P, Gutter C, Schnorr C (2005a) A variational approach for particle tracking velocimetry. Meas Sci Technol 16:1449–1458. doi:10.1088/0957-0233/16/7/007

Ruhnau P, Kohlberger T, Schnorr C, Nobach H (2005b) Variational optical flow estimation for particle image velocimetry. Exp Fluids 38:21–32. doi:10.1007/s00348-004-0880-5

Sanchez J, Meinhardt-Llopis E, Facciolo G (2013) TV-L_1 optical flow estimation. Image Process On Line 3:137–150. doi:10.5201/ipol.2013.26

Stark M (2013) Optical flow PIV: improving the accuracy and applicability of particle image velocimetry. ETH, Department of Mechanical and Process Engineering. https://books.google.cl/books?id=p92MnQEACAAJ

Strong DM, Chan TF (2003) Edge-preserving and scale-dependent properties of total variation regularization. Inverse Probl 19:165–187. doi:10.1088/0266-5611/19/6/059

Sun T, Teja A (2004) Density, viscosity and thermal conductivity of aqueous solutions of propylene glycol, dipropylene glycol, and tripropylene glycol between 290 K and 460 K. J Chem Eng Data 49:1311–1317. doi:10.1021/je049960h

Suter D (1994) Vector splines in computer vision. In: Proceedings of Australasian workshop thin plates, Sydney

Sutherland BR, Dalziel SB, Hughes GO, Linden PF (1999) Visualization and measurement of intertial waves by synthetic schlieren: part 1. Vertically oscillating cylinder. J Fluid Mech 390:93–126. doi:10.1017/S0022112099005017

Tokgoz S, Geisler R, van Bokhoven LJA, Wieneke B (2012) Temperature and velocity measurements in a fluid layer using background-oriented schlieren and PIV methods. Meas Sci Technol 23(115):302. doi:10.1088/0957-0233/23/11/115302

Turan J, Ovsenik L, Benca M (2002) Laboratory equipment type fiber optic refractometer. Radioengineering 11:27–32

Wang Z, Bovik AC (2009) Mean squared error: love it or leave it? A new look at signal fidelity measures. IEEE Signal Proc Mag 26:98–117. doi:10.1109/MSP.2008.930649

Wang Z, Bovik AC, Sheikh HR, Simoncelli EP (2004) Image quality assessment: from error visibility to structural similarity. IEEE Trans Image Process 13:600–612. doi:10.1109/TIP.2003.819861

Wedel A, Cremers D (2011) Stereo scene flow for 3D motion analysis, 1st edn. Springer, London. doi:10.1007/978-0-85729-965-9

Wedel A, Pock T, Zach C, Cremers D, Bischof H (2008) An improved algorithm for TV-L_1 optical flow. In: Proceedings of the Dagstuhl motion workshop, Dagstuhl Castle

Wildeman S, Lhuissier H, Sun C, Lohse D (2012) Inside a kettle. arXiv:12103693

Zach C, Pock T, Bischof H (2007) A duality based approach for real-time TV-L_1 Optical Flow. In: Hamprecht A, Schnorr C, Jahne B (eds) Pattern Recognition, chap 22, Springer, Berlin, pp 214–223